

# Coronary Artery Segmentation from Intravascular Optical Coherence Tomography Using Deep Capsules

Arjun Balaji,<sup>a</sup> Lachlan Kelsey,<sup>a,b</sup> Kamran Majeed,<sup>c,d,e</sup> Carl Schultz,<sup>c,d</sup> Barry Doyle<sup>a,b,f,g</sup>

- a. Vascular Engineering Laboratory, Harry Perkins Institute of Medical Research, QEII Medical Centre, Nedlands and Centre for Medical Research, The University of Western Australia, Perth, Australia.
- b. School of Engineering, The University of Western Australia, Perth, Australia.
- c. Department of Cardiology, Royal Perth Hospital, Perth, Australia.
- d. School of Medicine, The University of Western Australia, Perth, Australia.
- e. University of Ottawa Heart Institute, Ottawa, Ontario, Canada.
- f. Australian Research Council Centre for Personalised Therapeutics Technologies, Australia.
- g. British Heart Foundation Centre for Cardiovascular Science, The University of Edinburgh, UK.

## **Funding:**

We would like to thank the National Health and Medical Research Council (Grants APP1063986 and APP1083572), the Western Australia Department of Health Merit Award and the Royal Perth Hospital Medical Research Foundation.

## ABSTRACT

The segmentation and analysis of coronary arteries from intravascular optical coherence tomography (IVOCT) is an important aspect of diagnosing and managing coronary artery disease. However, automated, robust IVOCT image analysis tools are lacking. Current image processing methods are hindered by the time needed to generate these expert-labelled datasets and also the potential for bias during the analysis. Here we present a new deep learning method based on capsules to automatically produce lumen segmentations, built using a large IVOCT dataset of 12,011 images with ground-truth segmentations. This dataset contains images with both blood and light artefacts (22.8%), as well as noise from metallic (23.1%) and bioresorbable stents (2.5%). We trained our model on a dataset containing 9,608 images. We rigorously investigate design variations with respect to upsampling regimes and input selection and validate our deep learning model using 2,403 images. We show that our fully trained and optimized model achieves a mean Soft Dice Score of 97.11% (median of 98.2%), segments 200 IVOCT images in an acceptable timeframe of 12 seconds and outperforms current algorithms.

**Keywords:** Capsule Network, Coronary Artery, Deep Learning, Optical Coherence Tomography

## 1. INTRODUCTION

Atherosclerosis is a disease process that lies at the core of many cardiovascular pathologies and it is responsible for a large proportion of morbidity and mortality in both developing and developed countries. The process involves the accumulation of plaque in the walls of an artery and eventually can lead to partial or complete luminal obstruction. Atherosclerosis of coronary arteries is known as coronary artery disease and due to the high prevalence and clinical severity, is one of the world's largest public health concerns. Intravascular optical coherence tomography (IVOCT) is a contemporary high-resolution imaging tool that has proved useful in clinical settings, revealing the lumen geometry and dimensions, as well as vessel wall structure, with near microscopic features. For IVOCT data to be useful in a clinical environment the analysis of images needs to be accurate, fast and reproducible. The geometry of coronary arteries extracted from IVOCT can elucidate information about the luminal area, diameter and wall thickness, all of which are clinically relevant factors that inform the management of disease in the coronary catheterization laboratory. The production and analysis of these geometries has attracted much research, particularly in the automation of geometry extraction (Gaur et al., 2016; Huang et al., 2018; Roth et al., 2018; Tearney et al., 2006).

Early methods to produce these geometries were semi-automated, requiring software to produce lumen segmentations (Gaur et al., 2016; Toutouzas et al., 2015). However, these semi-automated methods are time and resource intensive and suffer from a range of reproducibility issues that are only discovered when analysis is being conducted (Toutouzas et al., 2015). This hinders the use of IVOCT analysis in time-pressured clinical situations.

Recent advancements in machine learning have stirred interest in new approaches to automated lumen segmentation. In 2015 there were several publications investigating the use of supervised machine learning techniques such as support vector machines and least squares regression to segment IVOCT data (Abdolmanafi et al., 2017; Guo et al., 2019; Kerkeni et al., 2016; Macedo et al., 2015). These efforts had varying levels of success, but were mainly limited due to the scarcity of training data and the intrinsic features present in coronary artery IVOCT, namely the guide wire's shadow and bifurcations of the coronary artery (Abdolmanafi et al., 2017; Kerkeni et al., 2016; Macedo et al., 2015). Newer works have used convolutional neural networks and linear regression techniques to annotate lumens using a points method, as opposed to a pixel-wise segmentation which have shown to be viable (Yong et al., 2017).

The rapid progress of machine learning has seen the emergence of a new field known as deep learning. Deep learning, particularly fully convolutional neural networks (FCN), demonstrated high performance results for segmentation tasks in non-medical imaging domains as early as 2014 (Roth et al., 2018; Shelhamer et al., 2016). However, FCN's are difficult to train due to the exponential increase in trainable parameters with an increase in network depth. This is important in the medical imaging domain as images are of a high resolution (often  $512 \times 512$  pixels or larger) which lead to extremely long training times and complex hyper-parameter tuning paradigms. Max-pooling was used to reduce the resolution of feature maps thus decreasing the parameter burden caused by increased network depth but introduced a new problem: loss of localization. The nature of max-pooling causes the network to lose part-whole relationships and makes it difficult for the network to preserve localisation information about objects in the scene. Ronneberger et al. (Ronneberger et al., 2015) proposed a solution to the localization. Their UNet architecture has a “down-branch” and an “up-branch” consisting of conventional convolution and max-pooling layers. The UNet promoted localization retention by implementing “skip connections” which concatenated corresponding feature maps from the “down” and “up” branches. This was a step forward in image segmentation, particularly in the medical imaging domain as the UNet performed well in multiple applications (Gessert et al., 2018; Huang et al., 2018; Miyagawa et al., 2018; Mortazi and Bagci, 2018; Ronneberger et al., 2015; Roth et al., 2018; Yong et al., 2017).

Sarbour et al. (2017) later laid out a new paradigm in image classification: the capsule. Capsule networks differ from FCN's and UNet's in two major ways; they store feature properties in vectors instead of scalars and layers are related via a dynamic routing algorithm instead of max-pooling. These vectors, or *capsules*, hold information about the orientation of the extracted feature in space, the magnitude of this feature, and other properties of the feature such as pose, skew and thickness. A novel non-linear squashing function introduced by Sarbour et al. scales these vectors so that their magnitude represents probabilities of features existing in their receptive field. However, their dynamic routing algorithm linked capsules in one layer to every capsule in the next layer, drastically restricting the size of images capsule networks could process.

LaLonde and Bagci (2018) then proposed CapsSeg, a capsule network modified for image segmentation of lung tissue in a CT dataset known as LUNA16 (Lung Nodule Analysis 2016) (Setio et al., 2017). One of the important changes introduced in this work was the locally constrained routing algorithm which only routed capsules in a layer to capsules in their neighborhood in the next layer. CapsSeg achieved start-of-the-art performance on the LUNA16 dataset and did so with a 95% reduction in parameters (LaLonde and Bagci, 2018).

In this work we apply the idea of capsules to coronary artery IVOCT lumen segmentation. In Section 2 we discuss the dataset and the model architecture, in Section 3 we present and discuss our findings and in Section 4 we present our conclusions.

## **2. METHODS**

In this work we apply a novel deep learning architecture that involves capsules to coronary artery IVOCT pullbacks which allows us to produce pixel-wise binary masks of coronary artery lumens. We refer to this algorithm as DeepCap. We investigate the effectiveness of 2 different upsampling regimes, we propose a new paradigm for model input selection, and we present a fully trained IVOCT segmentation model based on capsules.

### **2.1 Dataset**

The dataset we used to train our models was developed in house using IVOCT B-scans acquired as part of the MOTIVATOR Study (ACTRN:12615001234505). All images were acquired using the frequency domain OCT system (C7-XRTM OCT Intravascular Imaging System. St. Jude Medical, St. Paul, MN, USA). Briefly, a 2.7-Fr OCT imaging catheter (Dragonfly, Lightlab Imaging, Westford, MA, USA) was advanced over a standard 0.014 guide wire with the imaging marker sufficiently distal. Automated OCT pullback was performed using a speed of 20 mm/s during simultaneous iso-osmolar X-ray contrast medium (Visipaque 320, GE Healthcare, Buckinghamshire, U.K.) delivery through the coronary guide catheter. All the IVOCT images were anonymized and manually segmented offline using in-house software, where images were first segmented by one user and then verified by another user; these segmented images represent the binary ground-truth label. The dataset of 12,011 images contains blood and light artefacts (22.8% of images), as well as metallic (23.1%) and bioresorbable stents (2.7%). The size and quality of this dataset, with artefacts, enables the formation of a robust and reliable machine learning workflow. Once the dataset was compiled in its entirety, we randomly split it into two distinct sets; a training set (80% of total dataset) and a validation set (20%), with cases randomly assigned to either set, while ensuring the size ratio. The purpose of a validation set is to perform “mini-tests” per epoch to continuously monitor the progress of our network in an objective fashion. It is important to remember that the model is prohibited from learning when being run on the validation set. Transformations are not applied to the validation set, giving a more accurate representation of real-world use. The selection of these sets is done using a random sampler, and we present results from these experiments in Section 3.

## 2.2 Preprocessing

We feed DeepCap an input that comprises of some combination of three distinct images; an augmented input image, a 2-dimensional (2D) Gaussian derivative of the input image and an axial forward and backward difference image.

We transform the raw image data ( $360 \times 720$  pixels) that has been extracted by the imaging system software into Cartesian form before taking a central crop of  $300 \times 300$  pixels which has the effect of removing black bars from the borders of the image. This Cartesian  $300 \times 300$  pixel image represents a single *pre-augmented* input image. It has been shown (Hussain et al., 2017) that augmenting the training dataset of a deep learning model can improve its generalizability for image segmentation tasks and thus we apply a sequence of transforms on our *input* before presenting it to the model for training. These transforms, illustrated in Figure 1, are; a random crop of  $256 \times 256$  pixels, a horizontal reflection, a vertical reflection, a Gaussian blur ( $\alpha = 1$ ), a clockwise/counterclockwise rotation ( $0^\circ \leq \theta \leq 360^\circ$ ), and salt and pepper noise (Hussain et al., 2017).

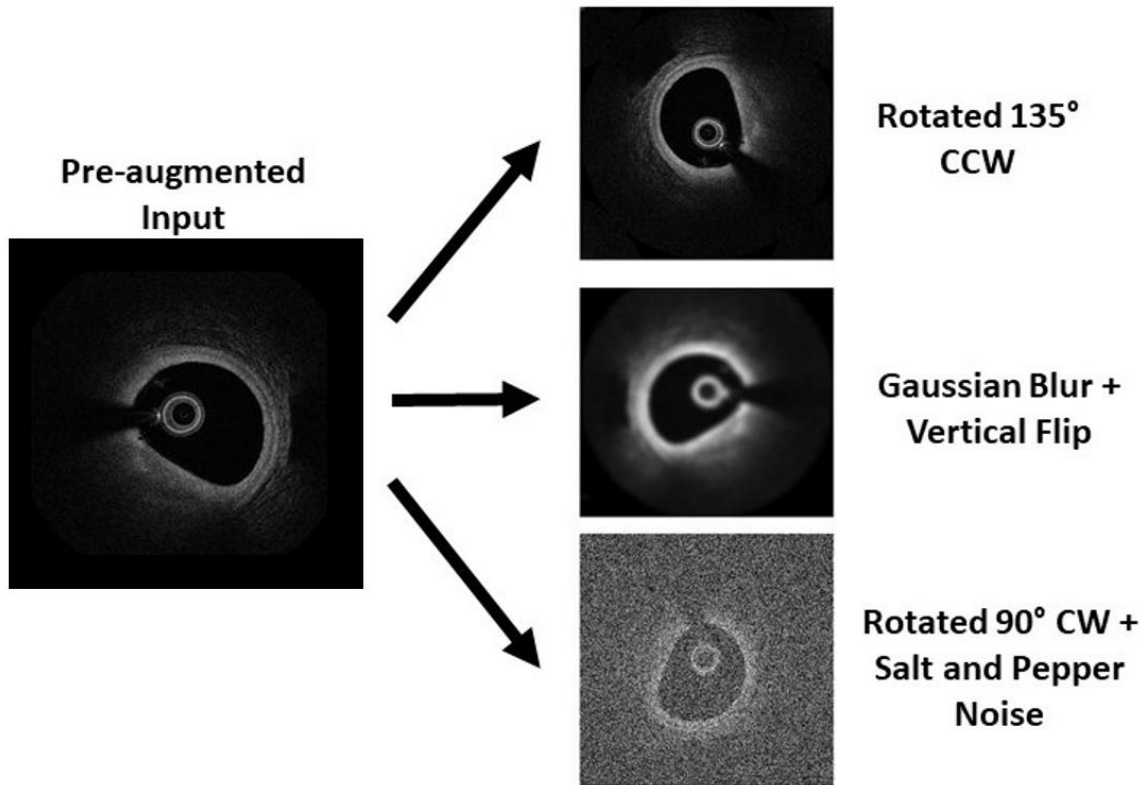


Figure 1: Three examples of how a raw input could be augmented before being presented to the model. This is for illustrative purposes; pictures are cropped to  $256 \times 256$ .

The random crop is always applied, while the other transformations are applied with a probability of 0.5 each. The model receives a completely new perspective of the training data every epoch due to the probabilistic application of these transforms, which improves the generality of the final model. We use the same random seed between experiments to force deterministic application of the transforms.

Secondly, we compute a 2D-Gaussian derivative of the input image which computes a combination of band-pass filtering and spatial derivatives (Koenderink and van Doorn, 1992). This is useful in the coronary artery IVOCT imaging domain because there is a scarcity of trainable data for the model, thus by providing a supplementary structure that removes background noise and provides some heuristic edge detection we can speed up training of the model and extract more high-level features from the training data.

Finally, we compute a forward and backward difference about the input image in the axial plane which can be expressed as,

$$\Delta X(z_0) = X(z_0 + \delta) - X(z_0 - \delta), \quad (1)$$

where  $X(z)$  is the image array at  $z$  and  $\delta$  is the distance between slices as reported by the IVOCT software. We believe this will allow the model to consider the behavior of the images in the locality of the image being segmented before making a prediction about the lumen geometry.

We performed experiments to investigate the model’s performance when given an input of either just the input image, the input image and the 2D-Gaussian derivative, the input image and the axial difference image and finally all three images.

It is important to note the difference between this approach and prior work in automated IVOCT segmentation. Previous work in this field has relied on semi-automated removal of image features such as the OCT guidewire shadow and artefacts; in extreme cases some images have been removed from the dataset due to acquisition artefacts or the lumen being out of frame (Abdolmanafi et al., 2017; Guo et al., 2019; Huang et al., 2018; Miyagawa et al., 2018). Our work has no such removal of features or images, resulting in a more rigorous and generalized model that lends itself to being used in clinical scenarios that are typically characterized by variability between IVOCT operators and software.

## 2.3 The Model Architecture

The model’s architecture, as illustrated in Figure 2, is reminiscent of the UNet’s with its downsampling

branch, upsampling branch and skip connections however there are several key differences. The first layer of the model is a conventional convolution operation that converts the input to a set of four feature maps each of which is a  $64 \times 64$  grid of 16 dimensional vectors. These vectors are known as the primary capsules. The convolution kernels that produce the primary capsules have randomly initialized weights and this is the only layer of the network that will not undergo dynamic routing (LaLonde and Bagci, 2018; Sabour et al., 2017). We will denote the shape of a set of capsules as  $(M, H, W, D)$  where  $M$  is the number of feature maps,  $H$  and  $W$  are the height and width of a feature maps respectively and  $D$  is the dimension of the capsule vectors.

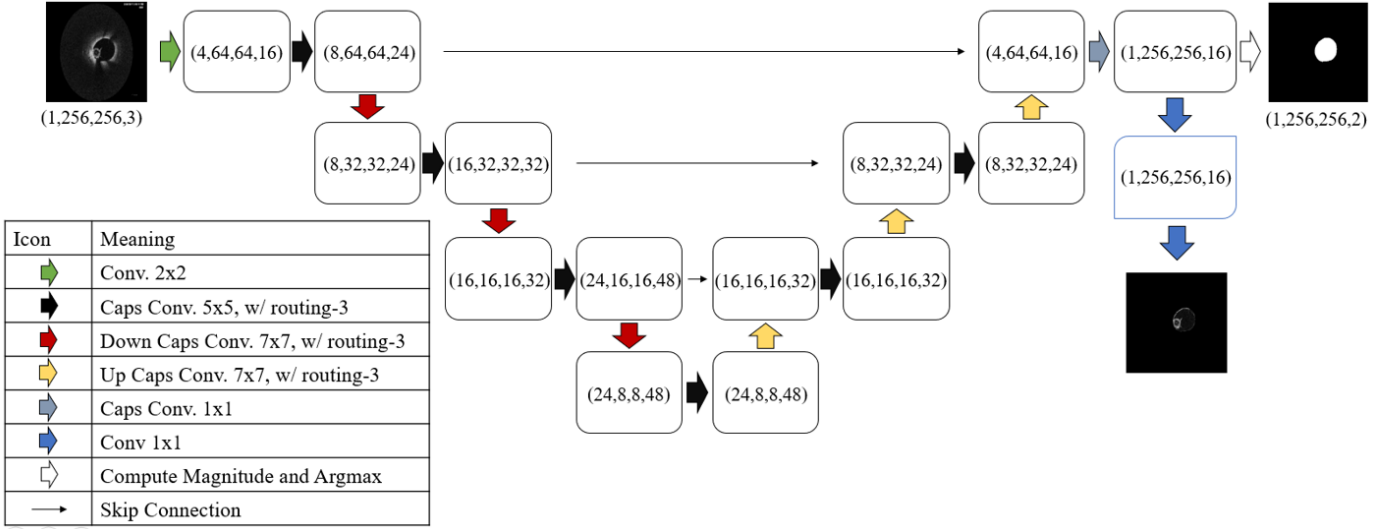


Figure 2: A schematic of the model's architecture that highlights how data flows through the various layers of our network. The legend explains the name of the layer, the kernel size (if applicable) and the amount of routing iterations (if applicable).

The first or 'down' portion of the network consists of the 3 layers, each of which is comprised of two separate capsule convolution modules and their associated routing schemes. The first of these modules takes in an input of shape  $(M^l, H^l, W^l, D^l)$  and outputs a tensor of shape  $(M^{l'}, H^l, W^l, D^{l'})$ , and the second of these modules takes in that output of shape  $(M^{l'}, H^l, W^l, D^{l'})$  and outputs a tensor to layer  $l + 1$  of shape  $(M^{l'}, H^{l''}, W^{l''}, D^{l'})$  where  $M^{l'}$ ,  $D^{l'}$ ,  $H^{l''}$  and  $W^{l''}$  are specified at each module. The values in our experiment are given in Figure2. It is useful to briefly describe the mechanics of the operations here, though they are detailed in (LaLonde and Bagci, 2018). In the first convolutional capsule module, we convolve the input tensor with a  $k^{l'} \times k^{l'}$  set of learned, nonlinear transformation matrices which produces  $M^{l'}$  prediction vectors that are  $D^{l'}$ -dimensional for each space on the  $H^l \times W^l$  grid. As illustrated in Figure 2 we used  $k^{l'} = 7$  which means that each set of prediction vectors sent to the next module has information about the 48 neighboring capsules. The second module works similarly but instead of altering



the number of feature maps or the dimension of the capsule vectors, we employ a stride in our convolution to downsample the feature maps. However, no information is wholly discarded during the downsampling because the kernel size of  $k^{l''}$  is larger than the stride size (in Figure 2, note that  $k^{l''} = 5$  but the *stride* = 2). At the end of each module we perform 3 iterations of the locally constrained dynamic routing algorithm as prescribed in (LaLonde and Bagci, 2018).

The second or ‘up’ portion of the network is characterized by two properties; upsampling of current feature maps and skip-connections that combine higher-level extracted features with lower-level extracted features. We have a choice of upsampling methods at our disposal and here we will compare transposed convolutional upsampling with bilinear interpolation. The motivation behind using bilinear interpolation to upsample feature maps is that others (LaLonde and Bagci, 2018; Sabour et al., 2017) show how capsules encode information about the thickness, pose and spatial orientation of objects in the image, it therefore would be reasonable to simply scale these feature maps to the size required for skip-connections. The use of transposed convolutions as an upsampling method is motivated by the strong results they have demonstrated in prior convolutional neural networks (LaLonde and Bagci, 2018; Ronneberger et al., 2015; Sabour et al., 2017). The upsampling methods are integrated into a convolutional capsule layer and are followed by three iterations of the locally constrained dynamic routing algorithm. After the upsampling module we employ our previously utilized convolutional capsule layers again to increase the depth of our network and allow it to extract more complex feature relationships from the training data.

After the input has gone through the ‘down’ and ‘up’ portions of our network we use two consecutive convolutional capsule layers to produce an output tensor of shape  $256 \times 256 \times 2$ . We would like the 1<sup>st</sup> channel to contain the probability that the pixel belongs to the background class and the 2<sup>nd</sup> channel to contain the probability that the pixel belongs to the lumen class. We impose this by applying a softmax function over the 3<sup>rd</sup> dimension of the tensor. During training, we compute a soft Dice loss and a binary cross entropy loss with this output and the target label. These losses were chosen because our model’s output map is an array of probabilities and our desired target is a binary array. Our choice of these two training losses is also grounded in literature as they have demonstrated state-of-the-art results in varied image segmentation tasks, particularly in the medical imaging domain (LaLonde and Bagci, 2018; Ronneberger et al., 2015; Zijdenbos et al., 1994; Zou et al., 2004). The soft Dice score (SDS) is a popular measure of similarity between the output masks from the model and ground-truth labels, in our experiments it quantifies how well the model can segment the IVOCT lumen in a given image, an easily interpretable metric. The soft Dice loss is was implemented with a multiplier of 0.1 to ensure the binary cross entropy

loss dominates during training, which is required for the loss to reliably converge. We apply an argmax function over the outputs last dimension to arrive at the final binary output.

To regularize the outputs of our network we implement a reconstruction branch on its tail. This entails adding two conventional convolutional layers to our network that receive the final capsule vector output of our network (see Figure 2) and outputs a reconstruction of the input image but for only the grid spaces that are part of the true target class. This helps the network retain all the relevant information required to produce accurate lumen segments which helps regularize our network and benefits its interpretability (LaLonde and Bagci, 2018). The reconstruction loss is added to the network loss with a scalar coefficient of 0.05 to ensure that the labelling losses dominate training.

## 2.4 Experiments

Our model was built on *PyTorch* and we used an Adam optimizer with a learning rate scheduler on plateau with a patience of 20 epochs and a multiplier of 0.1. We used GPU acceleration on a *Nvidia P100* to train our network with a batch size of 1. All preliminary experiments were run on 20 epochs and the final model was trained until the total loss stagnated for 20 epochs. Throughout the analysis of our model’s results we focus on three key metrics; the SDS, pixel accuracy and time taken. We have discussed the SDS and its benefits above. Pixel accuracy gives us an idea of how many pixels the model correctly labels, an important differentiation between this and the SDS is that pixel accuracy also informs us about how well the model can correctly segment background pixels, instead of lumen alone. Here it is important to recall that the output of our model is a binary one as we select the highest probability class for each pixel, meaning no thresholding is required to calculate many metrics. Finally, the time-taken to train the model is included in our analysis because continued training and edge-training are possible avenues to further improve the model in a clinical environment. The reason behind choosing these three metrics to quantify the model’s success is that they provide the clearest understanding of how the model performs, without obfuscating the results into a plethora of redundant values. Sensitivity, specificity, the Jaccard Index and F1 score are all related intrinsically to the soft Dice score and the pixel accuracy.

Our first experiment was to investigate the model’s performance under the bilinear interpolation and transposed convolution upsampling regimes. For these experiments both models were run on the same dataset split to eliminate any sample selection bias. The input selection was all three inputs.

Once we decided which upsampling to use we investigated which combination of inputs yields the best

model performance. The four experiments were: (i) only the input image, (ii) the input image and the 2D-Gaussian derivative, (iii) the input image and the axial difference map, and (iv) all three. Because the input image is present in all four experiments, we will henceforth term these experiments; IM, 2DG, ADM and ALL respectively. Again, the dataset split was the same for these experiments.

When we secured our desired input set, we tested our model on several different random dataset splits to demonstrate the validity of our model’s performance. Finally, we present the results of our final, fully trained capsule network and highlight some examples of the model in action.

### 3. RESULTS AND DISCUSSION

We performed several experiments to investigate the effectiveness of our model in different scenarios and with different metrics, which are explained below.

#### 3.1 Upsampling Paradigms

An important decision to make about our proposed model is the type of upsampling technique to use. We investigated using bilinear interpolation and transposed convolution to upsample feature maps in the second part of the network. Besides the upsampling method, both experiments used the exact same parameters - for example, the number of layers and kernel and batch size. The results are shown in Table 1.

*Table 1: Performance of the model in the bilinear interpolation and transposed convolution upsampling schemes. Data presented as mean  $\pm$  standard deviation.*

<b>Upsampling method</b>	<b>Bilinear</b>	<b>Transposed convolution</b>
soft Dice score	96.15 $\pm$ 2.57	96.53 $\pm$ 1.96
Pixel accuracy (%)	98.8 $\pm$ 0.88	98.98 $\pm$ 0.55
Training time (mins)	625	614

From Table 1 we can see that upsampling via transposed convolution is more effective than bilinear interpolation at maximizing soft Dice scores and pixel accuracy after 20 epochs of training. Despite marginal improvement in mean soft Dice and pixel accuracy from transposed convolution over bilinear interpolation, consistency between results was improved with transposed convolutions showing 31% and 60% smaller standard deviations than bilinear interpolation for soft Dice and pixel accuracy, respectively. These tight ranges in segmentation quality are due to the model learning how to upsample the feature maps

to best reduce the specified loss. Every training iteration leads to parameters in the convolution being reconfigured to give improved segmentations, whereas with bilinear interpolation the upsampling is not a learned feature, it is an algorithmic interpolation scheme.

Furthermore, training the transposed convolution network was 2% faster than the bilinear interpolation, which has practical significance when considering the final trained model will be run on hundreds of epochs. Though this sounds implausible as we are introducing more parameters with transposed convolution, it can be explained by several points. Firstly, transposed convolutions, like regular convolutions, are implemented in machine learning as a matrix multiplication operation which is efficient on the GPU, meanwhile bilinear interpolation is executed on the CPU and less efficient. Secondly, the feature maps we are upsampling are multidimensional and the bilinear interpolation method complicates exponentially with increasing dimensionality.

### **3.2 Determining Optimal Inputs**

We propose adding 2D-Gaussian derivatives and axial difference maps as inputs to the model to increase segmentation accuracy. To test this, we performed four experiments to identify which combination of the three proposed inputs (IVOCT image must be selected) would result in the best lumen segmentations. Like earlier, these experiments were conducted with the same dataset split and all model and environment parameters were kept constant, except the input data.

From the data in Table 2, we observe that the IM model (i.e. input image alone) performed poorly as it had the lowest mean pixel accuracy of 98.77% and the largest standard deviation in pixel accuracy of 0.98%. This inadequacy is because the model is not given information about slices in its axial vicinity and the model must learn the derivative kernels on its own. It is well documented that capsule networks quickly begin to delineate contrast change in their input maps, 2DG (i.e. input image and the 2D-Gaussian derivative) and ALL (i.e. input image, the 2D-Gaussian derivative and the axial difference map) models are explicitly given the 2D-derivatives of the input and as such the model requires less training iterations to learn about contrast change (Huang et al., 2018; Miyagawa et al., 2018; Ronneberger et al., 2015; Shelhamer et al., 2016; Zeiler and Fergus, 2013). This leads to comparatively worse segmentations with respect to models trained on just the image alone.

Table 2: A table summarizing the performance of 4 different input image schemes on soft Dice scores, pixel accuracy and training time. I (Image), G (2D-Gaussian Gradient), A (Axial Difference). Data presented as mean  $\pm$  standard deviation.

Inputs selected	Soft Dice score	Pixel accuracy (%)	Training time (mins)
I (IM)	96.13 $\pm$ 2.36	98.77 $\pm$ 0.98	497
I + G (2DG)	96.43 $\pm$ 2.52	98.94 $\pm$ 0.62	497
I + A (ADM)	95.88 $\pm$ 2.19	99.04 $\pm$ 0.74	498
I + G + A (ALL)	96.57 $\pm$ 2.22	98.98 $\pm$ 0.55	614

To determine the best performing regime out of 2DG, ADM and ALL, required a deeper analysis. All three models had similar performance in mean pixel accuracy, but ALL did demonstrate a meaningfully lower standard deviation of pixel accuracy at 0.55. To get a better understanding of how these models performed we examined the mean centred 95<sup>th</sup>-percentile of soft Dice scores for each model, shown in Figure 3. We find that ALL outperforms the other input experiments on the soft Dice metric as the 95%-percentile on test scores; (i) has a higher mean, (ii) is more tightly distributed, and (iii) has the highest sitting inter-quartile range. Table 2 also illustrates the approximately 22% longer training time for ALL compared to the other models. This is because the model’s input is composed of three images and as such the convolutional kernel in the primary capsules layer has more trainable weights, leading to longer training times. However, as the training time does not affect the processing speed for an end-use case of our segmentation algorithm, we are less sensitive to it than the quality of segmentations. As the ALL input selection regime provided the most desirable SDSs and rated highly on pixel accuracy, we continued our experiments using it.

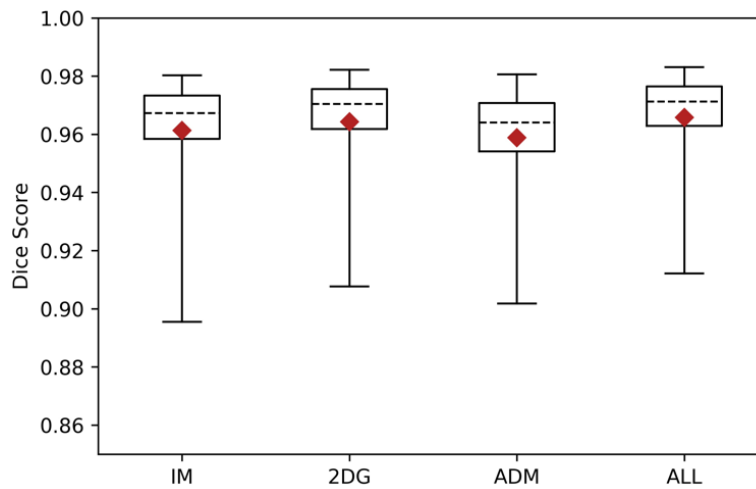


Figure 3: A series of box and whisker plots illustrating the 95<sup>th</sup>-percentile bound of soft Dice scores for each input regime. The dotted line marks the median and the red diamond marks the mean of the samples.

### 3.3 Splits

To demonstrate the robustness of our model, we performed experiments on five unique random splits of our dataset, also known as repeat random subsampling. This removes selection bias of the training and testing samples the model is exposed to while at the same time increasing the validity of our model’s performance. Furthermore, it imposes a fair distribution of the more difficult images, such as those with artefacts, bifurcations or stents, throughout the training and testing process (Hussain et al., 2017; Ronneberger et al., 2015; Setio et al., 2017; Taha and Hanbury, 2015; Zou et al., 2004). The results from these experiments are shown in Table 3. The robustness of the proposed network is demonstrated by the consistently high SDS and mean pixel accuracy and the low standard deviation of these two metrics. This is supported by Figure 4 which highlights the mean centered 95<sup>th</sup>-percentile of SDSs for each of the 5 splits. Figure 4 illustrates the consistently exemplar results by our model even in the context of varying exposure to training and testing data.

*Table 3: A table summarising the models test set results over 5 random splits of the dataset. Data presented as mean  $\pm$  standard deviation.*

<b>Splits</b>	<b>Soft Dice score</b>	<b>Pixel accuracy (%)</b>
0	96.58 $\pm$ 2.31	98.98 $\pm$ 0.57
1	96.66 $\pm$ 2.17	99.08 $\pm$ 0.65
2	96.53 $\pm$ 1.91	99.05 $\pm$ 0.71
3	96.56 $\pm$ 2.06	98.99 $\pm$ 0.76
4	96.58 $\pm$ 2.15	99.00 $\pm$ 0.75
<b>Average</b>	96.58 $\pm$ 2.06	99.02 $\pm$ 0.69

The mean pixel accuracy over the five testing splits was above 99% with a standard deviation of 0.69, a promising result that we shall discuss further in Section 3.4.

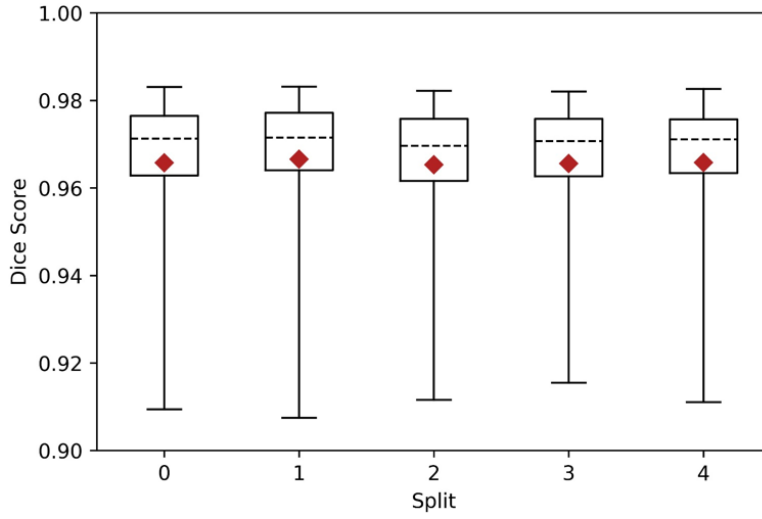


Figure 4: A series of box and whisker plots illustrating the 95th-percentile bound of dice scores for each of the 5 random dataset splits. The dotted line marks the median and the red diamond marks the mean of the samples.

### 3.4 Fully Trained Network

From our prior experiments we found that transposed convolution upsampling and providing the model with all three proposed inputs yielded the best lumen segmentations. As such the final fully trained model was implemented with transposed convolution upsampling and given all three proposed inputs; the image, 2D-Gaussian derivative and axial difference map. The results of the model outputs, as well as comparable models’ outputs in literature are presented in Table 4. This fully trained network is effective at producing high quality coronary artery lumen segmentations, even in challenging scenarios where artefacts and stents are present in the images.

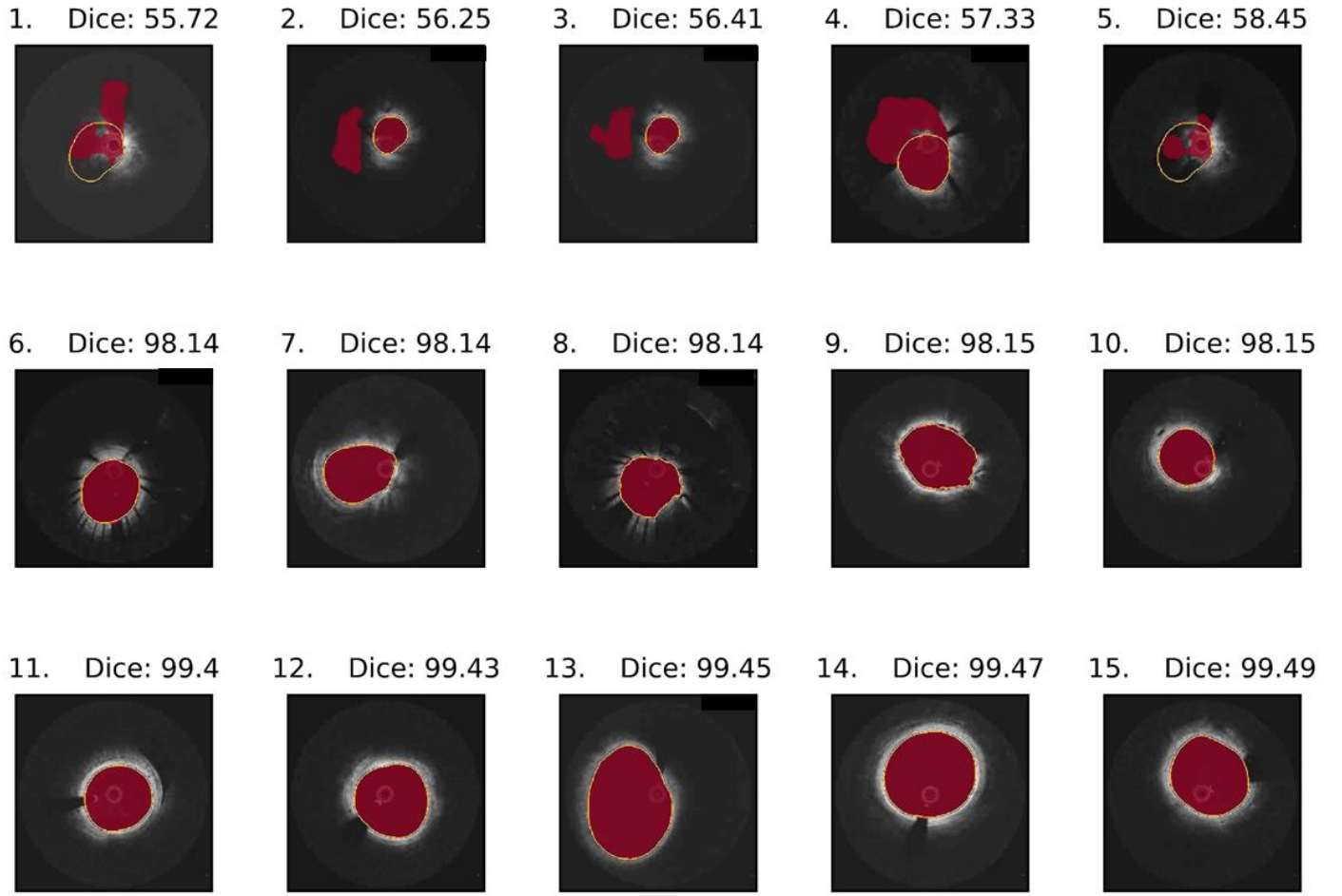
Table 4: Summary of dataset sizes and fully trained model’s performance over a single random split of the dataset relative to existing algorithms. Data presented as mean  $\pm$  standard deviation. N/A are undisclosed data in the publication. \* indicates median value.

	<b>DeepCap</b>	<b>Miyagawa et al.</b> (2018)	<b>Kim et al.</b> (2014)	<b>Moraes et al.</b> (2013)	<b>Tsantis et al.</b> (2012)	<b>Yong et al.</b> (2017)
Images (Total)	12,011	1,689	30	290	2710	19,027
Training	9,608	1,352	N/A	N/A	N/A	13,342
Validation	2,403	337	N/A	N/A	N/A	5,685
Pixel accuracy (%)	99.53 $\pm$ 0.69	98.93 $\pm$ 2.07	N/A	97.80 $\pm$ 2.16	93.70 $\pm$ 4.50	N/A
Sensitivity (%)	94.63 $\pm$ 6.30	96.92 $\pm$ 3.75	99.21 $\pm$ 0.51	99.29 $\pm$ 2.96	91.00 $\pm$ 1.00	N/A
Specificity (%)	99.48 $\pm$ 0.77	99.11 $\pm$ 2.19	99.70 $\pm$ 0.15	96.31 $\pm$ 2.88	96.00 $\pm$ 2.00	N/A
Soft Dice score	97.12 $\pm$ 4.22	94.34 $\pm$ 11.71	N/A	N/A	N/A	98.50*

The fully trained DeepCap model has a mean pixel accuracy of more than 99% with a very small standard deviation of 0.69%. Furthermore, the mean SDS is 97.12 with a standard deviation of 4.22 and the median SDS is 98.2. It should be noted that direct comparisons of research are difficult due to the differences in datasets however the dataset we have used is more than seven times larger than the one used by Miyagawa et al. (2018), 400 times larger than the one used by Kim et al. (2014), and 41 times larger than the one used by Moraes et al. (2013). This also doesn't consider the diversity of data which is pertinent in the context of coronary artery IVOCT lumen segmentation as the presence of artefacts, stents and plaque will all affect the validation performance of the model and its ability to generalise in real world applications. We purposely included all image data, irrespective of artefact and noise, so as to build a robust model that can handle typical IVOCT images encountered in the clinic. We hope that future work in this field present statistics about the contents of the dataset, similar to as we have in Section 2.

A comparison between DeepCap and the model presented by Miyagawa et al. illustrates the performance benefit afforded by a more comprehensive IVOCT dataset and the use of capsules over regular convolution (Miyagawa et al., 2018). Metrics of note are DeepCap's higher mean SDS (97.12 vs 94.34) and significantly smaller deviation of SDS (4.22 vs. 11.71) as well as a higher mean pixel accuracy (99.53 vs. 98.93). Training of this model was halted after 17 hours due to training loss stagnation as described in Section 2. This relatively short training time indicates that this network architecture can quickly learn the features present in IVOCT inputs, an important property as this could be useful in the future to quickly retrain the model or add new cases to its segmentation repertoire. When executed on a PC with an *AMD Ryzen 1600 central processing unit* and a *NVIDIA GTX 1070 (8GB)* graphics processor with a batch size of five, the model can segment 16.8 images per second on average, which means that the model can segment an entire 200 image B-scan in just under 12 seconds. This equates to an image being segmented every 0.06 seconds. When executed in CPU only mode with a batch size of one, the model can segment one image in five seconds. There is potential for this model to be run on a cloud server with GPU capability to produce segmentations in a timely manner. The speed of computation and the relatively cheap hardware required, combined with the robust segmentations produced, poises this model for future clinical application. Note that this quoted time also considers the time required to load the images, not just model computation time.

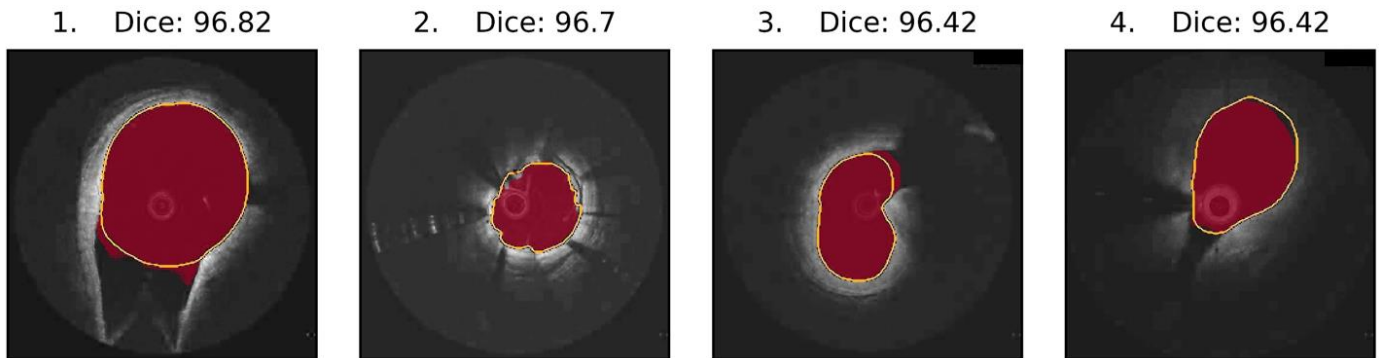




*Figure 5: Illustrative examples of the fully trained model's performance on validation data. The top row (1-5) are the five worst segmentations, the middle row (6-10) are the five median-centered segmentations and the bottom row (11-15) are the five best segmentations as measured by the soft Dice score (above each image). The model's segmentations are depicted by the red image masks and true lumen labels are depicted by the solid yellow outline.*

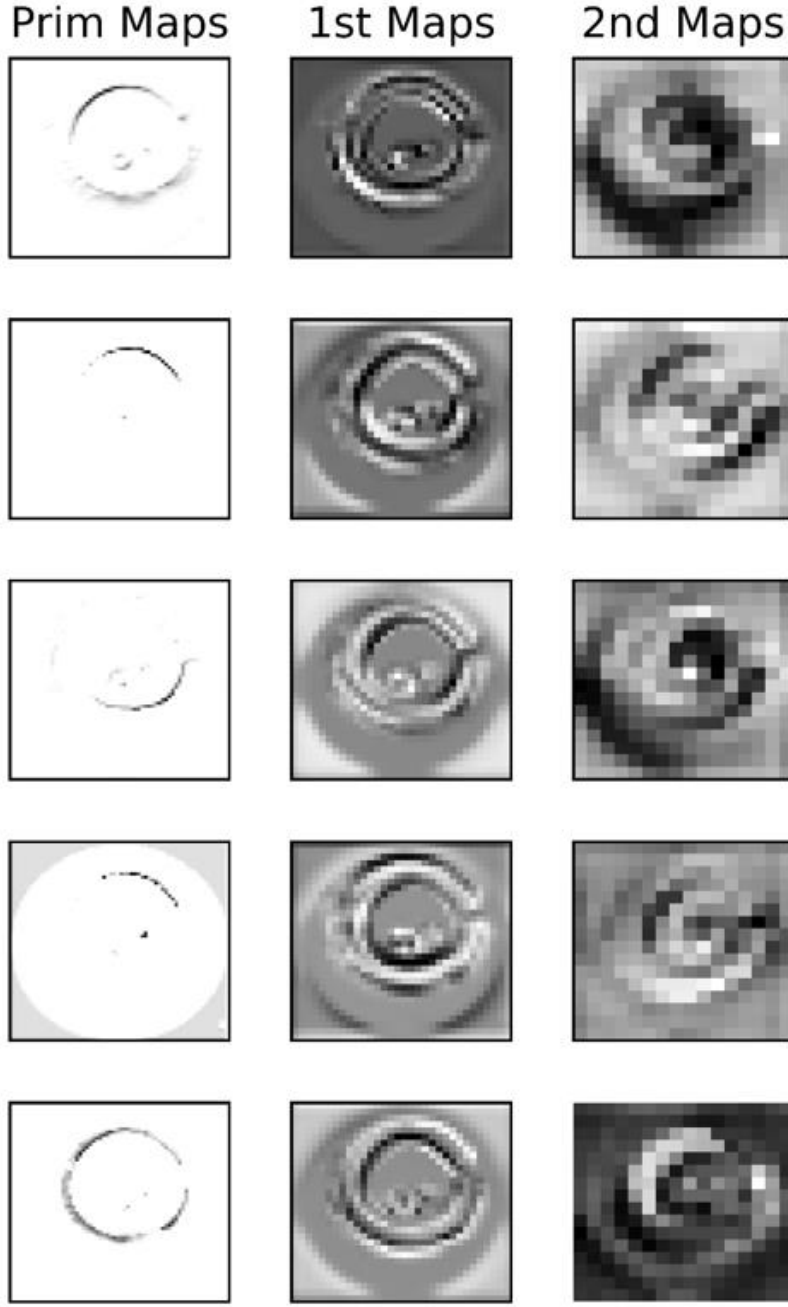
As shown in Figure 5(1-5), the images that the model finds difficult to segment are those that contain bifurcations, shadows or lumens that have an atypical shape. Furthermore, some of these images are from the same OCT-pullback, e.g. Figure 5(2-3), demonstrating how acquisition artefacts in one image are often visible in their locality and as such the model will have difficulty over a section of an IVOCT scan. We have shown the five worst segmentations for completeness, but segmentations this poor is exceedingly rare with Figure 5(1-5) being at least 9.27 standard deviations from the mean SDS. During our analysis we found that for images with an SDS greater than 93%, no human editing of the mask was necessary. In our test set, more than 94% of images segmented by the model had an SDS greater than 93%, meaning in a 200 image B-scan only 12 images on average would need some human editing. We expect that as we continue to train the model with more difficult cases and more fringe scenarios, this number will reduce further.

Figure 6 illustrates the robust segmentation potential of our fully trained model (DeepCap). These images demonstrate some of the more difficult segmentation scenarios as they contain more than one image artefact per image. We can see that that our model is achieving near mean accuracy on some of these images which has two implications; (i) we can expect the model to perform as expected in a clinical context where patients have stented segments and blood artefacts in their IVOCT images, and (ii) these masks will not require human editing as their SDS exceeds 93%.



*Figure 6: A sample of four images from the validation set that demonstrate the model's robust segmentation ability. (1,3,4) contain bifurcations and blood artefacts and (2) contains stent and blood artefacts. The model's segmentations are depicted by the red image masks and true lumen labels are depicted by the solid yellow outline.*

To demonstrate the type of features that the capsules extract from the input IVOCT images, we include a sample of feature maps from the down portion of the network in Figure 7. We chose an input that the model was effective at segmenting because it more easily elucidates the way the model works. We can see that in the primary capsule layer (Prim. Maps in Figure 7) the model is extracting very high-level features such as the different kind of curves and contrast changes. In the first capsule layer (1st Maps in Figure 7) the model is discerning more low-level image features such as the guidewire shadow and the central imaging source. We can also clearly see that the model recognizes the bounds of the circular IVOCT image. Finally, the second capsule layer (2nd Maps in Figure 7) identifies lower-still image features such as the gross location of the lumen and shadow. An interesting thing to note about these images is they look like a shadowed sphere; this indicates some of the generality gained by these networks due to the repeated linear transformations we apply to the input signal.



*Figure 7: A sample of extracted feature maps by the model from the down layer of the network. Each column of images is a small subset of the extracted feature maps, the exact number can be found in Figure 2. The input image was the same as Figure 5(10). Prim = primary capsule layer; 1<sup>st</sup> maps = first capsule layer; 2<sup>nd</sup> map = second capsule layer.*

In Figure 8 we present an example case from the validation set that compares our model's segmentation against two human ones; H1 being in the validation set, H2 being performed after the model was finalized and blinded from both the DeepCap prediction and H1. This case is the only OCT-pullback in the validation set containing images of a bioresorbable stent (51 images) and also contains a large bifurcation, making it time-consuming to perform precise manual segmentation (i.e. > 1 hour). The second human segmentation allows us to analyze how our model performs when we account for ground-truth

segmentation variability. Furthermore, as only 241 images containing bioresorbable stents were present in the training set (241/9,608), for these images the performance of the model is considered to be limited by the dataset. Figure 8 demonstrates that our model captures global and local characteristics of the human segmentations. We see that our model performs similar to humans when comparing vessel radii on a per-point basis in IVOCT lumen segmentation. The radius heat maps of H1, DeepCap and H2 are similar and show that even in the stented regions, the model can produce segmentations that yield radii measurements comparable to human segmentations. Figure 8 also shows that our model's segmentations yield similar cross-sectional areas to those of human segmentations. In the stented region, the model produces smoother outputs than the human segmentations, resulting in a slightly larger cross-sectional area between images 210 and 250.

There is significant scope for future work on automated IVOCT lumen segmentation using deep learning. For instance, our model ignores bifurcations and instead segments the lumen in images with bifurcations based on interpolation from previous frames. Nevertheless, we have demonstrated that capsules form the basis of an effective architecture for IVOCT segmentation because they are able to easily localize image features and relate those image features to output lumen segmentations. However, making our model more effective at segmenting fringe cases is important. In the future we will investigate a new training scheme where more difficult images are fed back into the model at training time so that the model is exposed to these more difficult images at a higher frequency. We are also investigating adding a model feature that predicts the potential accuracy for an input image. This would allow us to create an exclusion criterion and improve usability in a clinical setting.

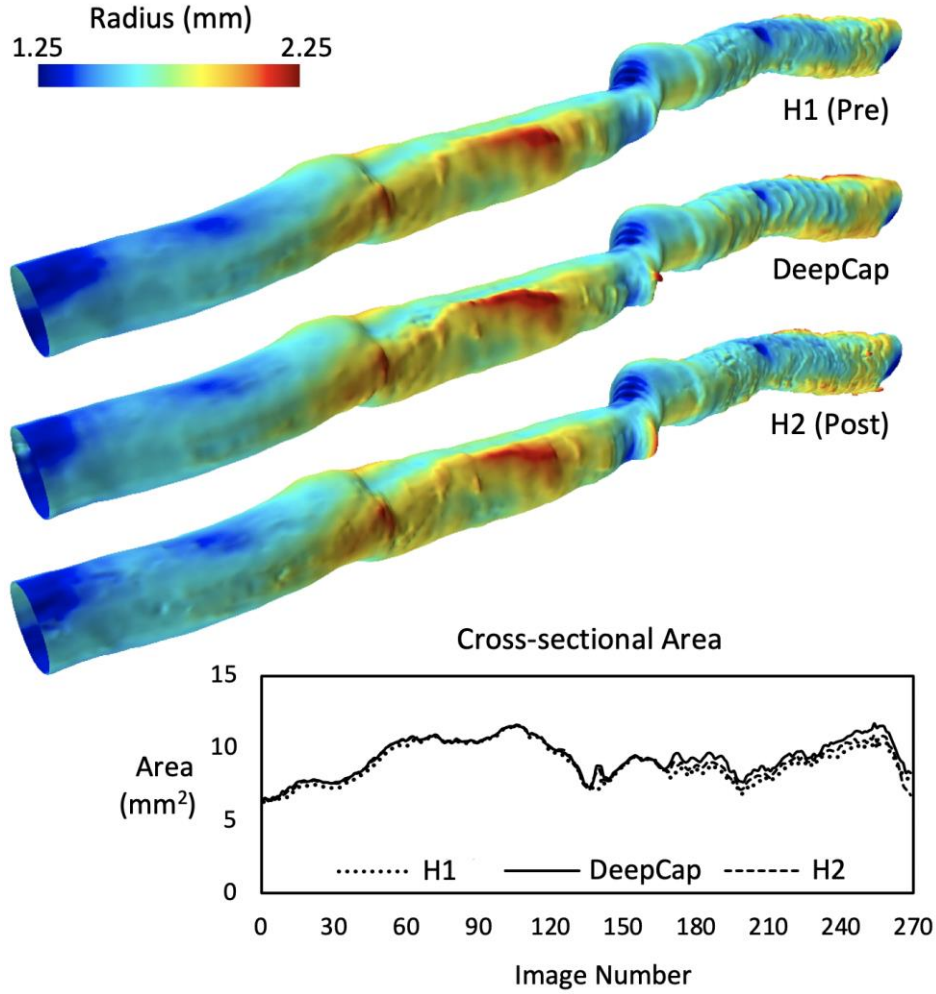


Figure 8: A comparison of our model (Prediction) vs. two human segmentations (H1, H2) for a case from our validation set. For each segmentation, the radius heat map illustrates the magnitude of displacement between the vessel-wall vertices and the lumen-mask centroids, computed for each image using the area-moment method. The plot compares the cross-sectional area ( $\text{mm}^2$ ) per image yielded by the various segmentations. The surfaces shown here are generated using a marching cubes algorithm at a voxel resolution of  $100\mu\text{m} \times 50\mu\text{m} \times 50\mu\text{m}$ . The radial heat maps are shown on smoothed surface meshes, obtained using STAR CCM+ (v13.06, Siemens): each surface mesh underwent a Laplacian smoothing operation where the vertices were re-projected to the initial surface.

#### 4. CONCLUSION

We propose a new deep learning model based on capsules as an accurate and efficient method of automatically segmenting coronary artery lumens from IVOCT. We trained our model on one of the largest expert-labelled coronary artery IVOCT datasets in the medical machine learning literature. In our analysis we investigated several different design schemes for the internal upsampling regime of the model and model input selection. We found that our model performed the best, as measured by mean pixel accuracy and soft Dice score, when we used the transposed convolution upsampling scheme and gave the model the image, and a corresponding 2D-Gaussian derivative and axial difference map, as the model inputs. We also

demonstrated the robustness of our model with the above designs against five unique dataset splits. Finally, we present our fully trained model, which with our optimal design features scored a pixel accuracy over 99% on our test dataset. Our model demonstrates the potential for capsules as a basis for IVOCT lumen segmentation models and we show that providing the model with local spatial information does impact performance. We designed the model with a clinical use case in mind and as such the model doesn't require image modification or exclusion prior to being able to output segments. Furthermore, the model performs fast, being able to segment an entire 200 image B-scan in about 12 seconds on the current hardware. Compared to the existing methods, our novel model of automated coronary segmentation will provide the critical luminal information much faster, during time-dependent, life-saving percutaneous coronary intervention procedures.

## 5. REFERENCES

- Abdolmanafi, A., Duong, L., Dahdah, N., Cheriet, F., 2017. Deep feature learning for automatic tissue classification of coronary artery using optical coherence tomography. *Biomed Opt Express* 8, 1203-1220.
- Gaur, S., Ovrehus, K.A., Dey, D., Leipsic, J., Botker, H.E., Jensen, J.M., Narula, J., Ahmadi, A., Achenbach, S., Ko, B.S., Christiansen, E.H., Kaltoft, A.K., Berman, D.S., Bezerra, H., Lassen, J.F., Norgaard, B.L., 2016. Coronary plaque quantification and fractional flow reserve by coronary computed tomography angiography identify ischaemia-causing lesions. *Eur Heart J* 37, 1220-1227.
- Gessert, N., Lutz, M., Heyder, M., Latus, S., Leistner, D.M., Abdelwahed, Y.S., Schlaefer, A., 2018. Automatic Plaque Detection in IVOCT Pullbacks Using Convolutional Neural Networks. *IEEE Transactions on Medical Imaging* 38, 426-434.
- Guo, X., Tang, D., Molony, D., Yang, C., Samady, H., Zheng, J., Mintz, G.S., Maehara, A., Wang, L., Pei, X., Li, Z.-Y., Ma, G., Giddens, D.P., 2019. A Machine Learning-Based Method for Intracoronary OCT Segmentation and Vulnerable Coronary Plaque Cap Thickness Quantification. *International Journal of Computational Methods* 16.
- Huang, W., Huang, L., Lin, Z., Huang, S., Chi, Y., Zhou, J., Zhang, J., Tan, R., Zhong, L., 2018. Coronary Artery Segmentation by Deep Learning Neural Networks on Computed Tomographic Coronary Angiographic Images, 2018 40th Annual International Conference of the IEEE Engineering in Medicine and Biology Society (EMBC), pp. 608-611.
- Hussain, Z., Gimenez, F., Yi, D., Rubin, D., 2017. Differential Data Augmentation Techniques for Medical Imaging Classification Tasks. *AMIA ... Annual Symposium Proceedings/AMIA Symposium*, 979-984.
- Kerkeni, A., Benabdallah, A., Manzanera, A., Bedoui, M.H., 2016. A coronary artery segmentation method based on multiscale analysis and region growing. *Comput Med Imaging Graph* 48, 49-61.

- Kim, H.M., Lee, S.H., Lee, C., Ha, J., Yoon, Y., 2014. Automatic lumen contour detection in intravascular OCT images using Otsu binarization and intensity curve, 2014 36th Annual International Conference of the IEEE Engineering in Medicine and Biology Society, pp. 178-181.
- Koenderink, J.J., van Doorn, A.J., 1992. Generic neighborhood operators. *IEEE Transactions on Pattern Analysis and Machine Intelligence* 14, 597-605.
- LaLonde, R., Bagci, U., 2018. Capsules for Object Segmentation, arXiv e-prints.
- Macedo, M.M., Guimaraes, W.V., Galon, M.Z., Takimura, C.K., Lemos, P.A., Gutierrez, M.A., 2015. A bifurcation identifier for IV-OCT using orthogonal least squares and supervised machine learning. *Comput Med Imaging Graph* 46 Pt 2, 237-248.
- Miyagawa, M., Costa, M.G.F., Gutierrez, M.A., Costa, J.P.G.F., Filho, C.F.F.C., 2018. Lumen Segmentation in Optical Coherence Tomography Images using Convolutional Neural Network, 2018 40th Annual International Conference of the IEEE Engineering in Medicine and Biology Society (EMBC), pp. 600-603.
- Moraes, M.C., Cardenas, D.A., Furuie, S.S., 2013. Automatic lumen segmentation in IVOCT images using binary morphological reconstruction. *Biomedical Engineering Online* 12, 78.
- Mortazi, A., Bagci, U., 2018. Automatically Designing CNN Architectures for Medical Image Segmentation. Springer International Publishing, Cham, pp. 98-106.
- Ronneberger, O., Fischer, P., Brox, T., 2015. U-Net: Convolutional Networks for Biomedical Image Segmentation. Springer International Publishing, Cham, pp. 234-241.
- Roth, H.R., Shen, C., Oda, H., Oda, M., Hayashi, Y., Misawa, K., Mori, K., 2018. Deep learning and its application to medical image segmentation, arXiv e-prints.
- Sabour, S., Frosst, N., Hinton, G., 2017. Dynamic Routing Between Capsules, arXiv e-prints.
- Setio, A.A.A., Traverso, A., de Bel, T., Berens, M.S.N., Bogaard, C.V.D., Cerello, P., Chen, H., Dou, Q., Fantacci, M.E., Geurts, B., Gugten, R.V., Heng, P.A., Jansen, B., de Kaste, M.M.J., Kotov, V., Lin, J.Y., Manders, J., Sonora-Mengana, A., Garcia-Naranjo, J.C., Papavasileiou, E., Prokop, M., Saletta, M., Schaefer-Prokop, C.M., Scholten, E.T., Scholten, L., Snoeren, M.M., Torres, E.L., Vandemeulebroucke, J., Walasek, N., Zuidhof, G.C.A., Ginneken, B.V., Jacobs, C., 2017. Validation, comparison, and combination of algorithms for automatic detection of pulmonary nodules in computed tomography images: The LUNA16 challenge. *Medical Image Analysis* 42, 1-13.
- Shelhamer, E., Long, J., Darrell, T., 2016. Fully Convolutional Networks for Semantic Segmentation, arXiv e-prints.
- Taha, A.A., Hanbury, A., 2015. Metrics for evaluating 3D medical image segmentation: analysis, selection, and tool. *BMC Med Imaging* 15, 29.
- Tearney, G.J., Jang, I.K., Bouma, B.E., 2006. Optical coherence tomography for imaging the vulnerable plaque. *J Biomed Opt* 11, 021002.
- Toutouzas, K., Chatzizisis, Y.S., Riga, M., Giannopoulos, A., Antoniadis, A.P., Tu, S., Fujino, Y., Mitsouras, D., Doulaverakis, C., Tsampoulatis, I., Koutkias, V.G., Bouki, K., Li, Y., Chouvarda, I., Cheimariotis, G.,

Maglaveras, N., Kompatsiaris, I., Nakamura, S., Reiber, J.H., Rybicki, F., Karvounis, H., Stefanadis, C., Tousoulis, D., Giannoglou, G.D., 2015. Accurate and reproducible reconstruction of coronary arteries and endothelial shear stress calculation using 3D OCT: comparative study to 3D IVUS and 3D QCA. *Atherosclerosis* 240, 510-519.

Tsantis, S., Kagadis, G.C., Katsanos, K., Karnabatidis, D., Bourantas, G., Nikiforidis, G.C., 2012. Automatic vessel lumen segmentation and stent strut detection in intravascular optical coherence tomography. *Medical Physics* 39, 503-513.

Yong, Y.L., Tan, L.K., McLaughlin, R., Chee, K.H., Liew, Y.M., 2017. Linear-regression convolutional neural network for fully automated coronary lumen segmentation in intravascular optical coherence tomography. *Journal of Biomedical Optics* 22, 126005.

Zeiler, M.D., Fergus, R., 2013. Visualizing and Understanding Convolutional Networks, arXiv e-prints.  
Zijdenbos, A.P., Dawant, B.M., Margolin, R.A., Palmer, A.C., 1994. Morphometric analysis of white matter lesions in MR images: method and validation. *IEEE Transactions on Medical Imaging* 13, 716-724.

Zou, K.H., Warfield, S.K., Bharatha, A., Tempany, C.M.C., Kaus, M.R., Haker, S.J., Wells, W.M., 3rd, Jolesz, F.A., Kikinis, R., 2004. Statistical validation of image segmentation quality based on a spatial overlap index. *Acad Radiol* 11, 178-189.